Title

Dynamics of Dinitrosyl Iron Complex (DNIC) Formation with Low Molecular Weight Thiols.

Journal

Inorganic chemistry, 58(19)

ISSN

0020-1669

Authors

Truzzi, Daniela R

Augusto, Ohara

Iretskii, Alexei V

et al.

Publication Date

2019-10-01

DOI

10.1021/acs.inorgchem.9b02338

Dynamics of Dinitrosyl Iron Complex (DNIC) Formation with Low Molecular Weight Thiols

Daniela R. Truzzi*[a,b], Ohara Augusto[b], Alexei V. Iretskii[c], Peter C. Ford*[a]

[a] Department of Chemistry and Biochemistry, University of California, Santa Barbara, Santa Barbara, CA, 93106-9510, USA.

[b] Departamento de Bioquímica, Instituto de Química de São Paulo, Universidade de São Paulo, Caixa Postal 26077, CEP05513-970, São Paulo, SP, Brasil.

[c] Department of Chemistry and Environmental Sciences, Lake Superior State University, Sault Sainte Marie, Michigan, 49783 USA

KEYWORDS: nitric oxide, dinitrosyl iron complex, cysteine, glutathione, biothiols, Roussin's ester

Supporting Information Placeholder

ABSTRACT: Dinitrosyl iron complexes (DNICs) are ubiquitous in mammalian cells and tissues producing nitric oxide (NO) and have been argued to play key physiological and pathological roles. Nonetheless, the mechanism and dynamics of DNIC formation in aqueous media remain only partially understood. Here, we report a stopped-flow kinetics and density functional theory (DFT) investigation of the reaction of NO with ferrous ions and the low molecular weight thiols glutathione (GSH) and cysteine (CysSH) as well as the peptides WCGPC and WCGPY to produce DNICs in pH 7.4 aqueous media. With each thiol, a two-stage reaction pattern is observed. The first stage involves several rapidly established pre-equilibria leading to a ferrous intermediate concluded to have the composition $Fe^{II}(NO)(RS)_2(H_2O)_x$ (**C**). In the second stage, **C** undergoes rate-limiting, unimolecular auto-reduction to give thiyl radical ($RS^{\bullet}$) plus the mono-nitrosyl Fe(I) complex $Fe^{I}(NO)(RS)(H2O)_x$ following the reactivity order CysSH > WCGPC > WCGPY > GSH. Time course simulations using the experimentally determined kinetics parameters demonstrate that, at a NO flux characteristic of inflammation, DNICs will be rapidly formed from intracellular levels of ferrous iron and thiols. Furthermore, the proposed mechanism offers a novel pathway for S-nitroso thiol (RSNO) formation in biological environment.

INTRODUCTION

Nitric oxide (NO) is an endogenously produced diatomic radical that is bioregulatory to many mammalian physiological/pathological functions.[1–3] Although NO is a free radical, its reactivity in biological media is selective toward other radicals and transition metal centers.[2,4,5] For example, the reactions of NO with superoxide ion ($O_2^{\bullet-}$) to give peroxynitrite ($ONOO^-$/ONOOH) and with thiyl radicals ($RS^{\bullet}$) to give S-nitroso thiols (RSNO) are nearly diffusion-limited,[6,7] while reactions with heme proteins are also well characterized.[1,8,9]

Less well understood is the reaction of NO with non-heme ferrous ions from the intracellular chelatable iron pool and low molecular weight or protein thiols to form dinitrosyl iron complexes.[10–12] Dinitrosyl iron complexes, which are also formed from NO reactions with Fe_4S_4 iron sulfur cluster proteins,[13,14] have been proposed to be the most abundant NO-derived adduct in cells exposed to either physiological or pathological concentrations of NO.[15] Furthermore, there is a growing interest in potential therapeutic applications of dinitrosyl iron complexes.[16,17]

Mononuclear dinitrosyl iron complexes (DNICs) display a characteristic EPR signal (g ~ 2.03), that was first observed as early as 1965 in cells and tissues exposed to NO.[10,18–20] Dinuclear dinitrosyl iron complexes known as Roussin's red salt esters (RSEs)[20–23] can also occur, although these are EPR-inactive and thus more difficult to detect in a biological milieu. The equilibrium between DNIC and RSE species is pH and thiol concentration dependent (eq. 1).[24,25]

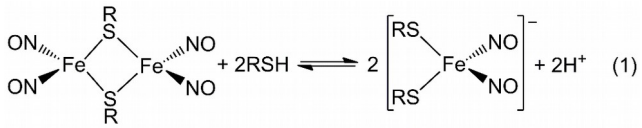

RSE (S = 0) **DNIC** (S = 1/2)

Although their physiological roles are not fully understood, dinitrosyl iron complexes have been proposed to be NO reservoirs and carriers due to their greater physiological life-times relative to molecular NO.[26–29] Also, DNIC formation may play a defensive role by reducing the availability of Fe(II) and NO-mediated oxidations.[30,31] In murine macrophage cells, the increase of DNIC levels were

shown to be concomitant to increased RSNO levels, leading to the suggestion that DNICs are able to promote nitrosation of biothiols.[32] In this context, we have recently utilized trapping techniques and EPR detection to identify thiyl radicals as co-products of dinitrosyl iron complex formation.[33] Thiyl radical generation in a NO rich environment would result in RSNO formation,[7] thereby offering a possible rationale for the observations in cells.

We report here a stopped-flow kinetics and density functional theory (DFT) investigation of dinitrosyl iron complex assembly from NO, Fe(II) and different biothiols in pH 7.4 aqueous media. Of particular interest is the tripeptide ECG, that is, glutathione (GSH). Given its prevalence in the cytosol (2-10 mM), the glutathione DNIC derivative $[Fe(NO)_2(GS)_2]^-$ is likely to be the major low molecular weight DNIC in mammals. A previous report from this laboratory probed the kinetics of analogous reactions with cysteine (CysSH);[25] here we reexamine and extend the studies with CysSH using upgraded instrumentation. Lastly, we describe stopped-flow studies of analogous reactions with the peptides WCGPC and WCGPY (Fig. 1) to evaluate whether a second coordinating residue (cysteine and tyrosine, respectively) has an impact on the kinetics of DNIC formation. Notably, the WCGPC motif is found in the active site of thiol based redox enzymes, such as thioredoxins, glutaredoxins, and protein disulfide isomerases.[34-36]

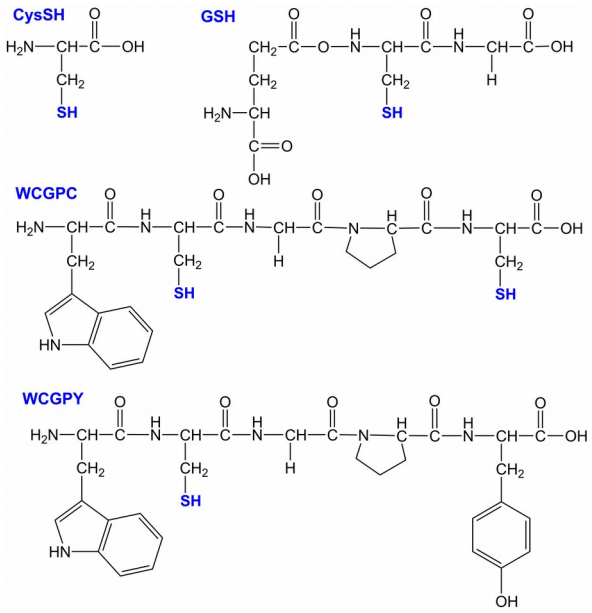

Figure 1. Formulas for cysteine (CysSH), glutathione (GSH), WCPGC and WCGPY.

RESULTS

The present study used the thiols GSH, CysSH, WCGPC or WCGPY, aqueous ferrous sulfate and purified NO gas to prepare the relevant solutions for kinetics experiments. In discussing the resulting data, the total concentration of the thiol molecules $[RSH]_{tot}$ refers to the sum of the RSH and its conjugate base RS^- after mixing. Correspondingly, $[Fe]_{tot}$ and $[NO]_{tot}$ refer to the total concentrations of all forms of these species upon mixing. Most studies were carried out in HEPES buffer solutions at pH 7.4 by stopped-flow mixing of a buffered solution containing Fe(II) and RSH with a second buffered solution containing NO.

Dinitrosyl iron complex formation with GSH

The reaction between Fe(II), NO and GSH is quite fast with dinitrosyl iron complex assembly being completed on a time scale of seconds. Therefore, the changes in the electronic spectra accompanying this transformation were followed in a stopped-flow spectrophotometer equipped with photodiode array (PDA) and photomultiplier tube (PMT) detectors. Figure 2 displays representative temporal absorption spectra subsequent to mixing Fe(II) (0.09 mM), NO (0.93 mM) and GSH (1.8 mM) at pH 7.4 and 298 K. The overall process observed spectrally can be partitioned into two time regimes. During the phase 1 (Fig. 2a), low-intensity absorption bands at 350 and ~450 nm are immediately observed at 2 ms and both continue to grow over the next few ms. The absorption spectrum subsequently evolves over the first 100 ms into a single strong band with a λ_{max} at 350 nm. During this latter stage, an isosbestic point at 415 nm develops as the broad shoulder at ~450 nm recedes. Notably, the rise and then fall of the latter absorbance clearly indicates that, even in the first 100 ms, several reactions are occurring, perhaps sequentially.

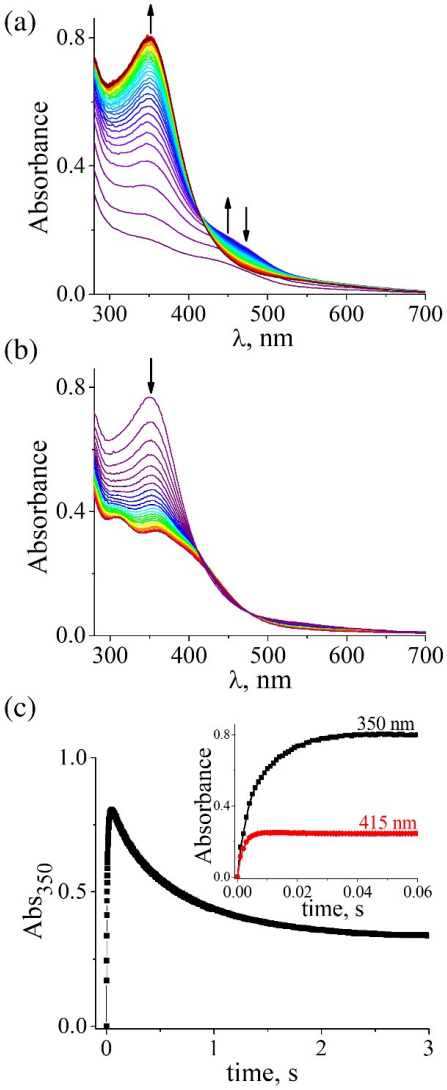

Figure 2. Temporal spectral changes upon stopped-flow mixing of GSH, NO and Fe(II) in pH 7.4 aqueous solution. (a) Temporal absorption spectra for a solution containing Fe(II) (0.090 mM), NO (0.93 mM) and GSH (1.8 mM) acquired from 2 to 100 ms after mixing (phase 1). (b) Temporal spectra for the same solution from 100 ms to 3 s (phase 2). (c) Optical density changes at 350 nm and at 415 nm recorded after stopped-flow mixing of comparable solutions at the same initial concentrations. Conditions: The buffer was HEPES (200 mM); the temperature was 298 K.

During the slower phase 2 (Fig. 2b), the intensity of the 350 nm band decreases exponentially within a few seconds, and new absorption bands with maxima at 310 and 360 nm and a shoulder at 420 nm become evident and remain stable for minutes. This phase displays apparent isosbestic points maintained at 415 nm and ~475 nm. The final spectrum seen in this Figure 2b is consistent with the formation of a mixture of RSE (characteristic bands at 310 and 360 nm) and DNIC (broad band at ~400 nm).[25,37] The final spectrum of a comparable product solution at higher $[GSH]_{tot}$ is shown in the Supporting Information (SI) Figure S1a. As discussed below, the presence of a DNIC component was confirmed by recording the characteristic g = 2.03 EPR signal in product solutions.

Figure 2c shows the absorbance changes specifically at 350 nm or at 415 nm for comparable reaction systems. It is notable that the absorbance at 415 nm, which corresponds to an isosbestic point, achieves a steady-state value within 10 ms. In contrast, the absorbance at 350 nm takes longer (40 ms) to reach a maximum value during phase 1, and then decays during phase 2.

None of the mentioned temporal absorptive changes were seen upon mixing analogous solutions of Fe(II) and GSH (0.09 mM and 1.8 mM, respectively) without NO or Fe(II) and NO (0.09 mM and 0.93 mM, respectively) without GSH (SI Fig. S2). The solution of Fe(II) and GSH gave a very weak and indistinct absorbances, while the solution containing only Fe(II) and NO displayed two weak bands at 340 and 450 nm. The latter spectrum is consistent with that reported by Wanat et al[38] for the complex $Fe^{II}(NO)^{2+}_{(aq)}$ (**A**) with band maxima at 336 nm (ε = 440 M^{-1} cm^{-1}) and 451 nm (265 M^{-1} cm^{-1}). These workers also demonstrated that **A** is formed rapidly and reversibly with a K_{NO} of 0.44 × 10^3 M^{-1} (eq. 2). Thus, under the experimental conditions used here, this equilibrium is established in less than one millisecond. Neither of the spectra presented in SI Figure S2 would contribute significantly to the strong absorbance seen in Figure 2.

The mechanism(s) for formation of mono- and/or bi-nuclear dinitrosyl iron complexes from a solution containing initially Fe(II), NO and GSH must involve a number of steps including several ligand substitutions into the iron coordination sphere as well as reduction of Fe(II) (formally) to Fe(I).[39] In previous studies of analogous reactions with CysSH, the model for dinitrosyl iron complex formation shown in Scheme 1 was proposed.[25] In this model, the rate-limiting step (phase 2) was suggested to be the spontaneous, unimolecular autoreduction of a mono-nitrosyl Fe(II) species $Fe^{II}(NO)(RS)_2$ (**C**) to give a mono-nitrosyl Fe(I) species $Fe^{I}(NO)(RS)$ (**D**) and thiyl radicals ($RS^{\bullet}$). Subsequent fast reactions would give the final products. In a recent communication,[33] this model was reinforced by the EPR identification of a mono-nitrosyl iron(I) intermediate and thiyl radicals formation during the time frame of phase 2. The ensuing analysis of the kinetics and temporal spectral changes described in the present article further evaluates the viability of this mechanism.

Scheme 1. Model for formation of DNIC and RSE from Fe(II), RSH and NO in aqueous media. Black arrows represent phase 1 while blue arrows represent reactions taking place during phase 2

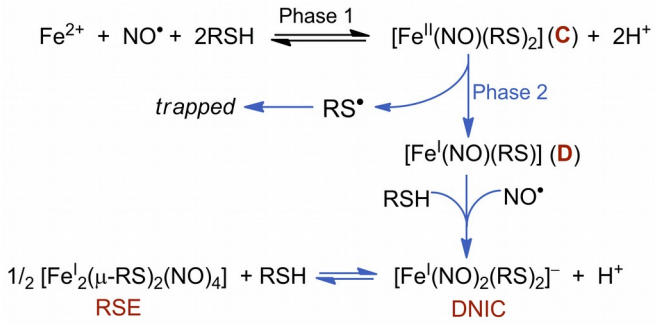

As predicted by Scheme 1, the phase 2 reaction displays first-order kinetics under a variety of conditions (different $[Fe(II)]_{tot}$, $[GSH]_{tot}$, $[NO]_{tot}$ and pH). Examples of the exponential decays from which the observed first order rate constants k_{obs} were obtained are shown in SI Figure S3. The limiting reactant in this system is ferrous iron, so after initial fast absorbance changes corresponding to phase 1, the instantaneous concentration of species **C** is dependent on $[Fe(II)]_{tot}$, $[GSH]_{tot}$, $[NO]_{tot}$ and pH (SI Figs. S4 & S5). Notably, at sufficiently high concentrations of GSH and NO, virtually all the Fe(II) is rapidly converted to **C** during phase 1.

The exponential decay of absorption curves at 350 nm (Abs_{350}) is related to the unimolecular decay of **C** (k_{rl}) according to an intricate relationship dependent on the concentrations of the other reagents present as indicated by eqs 3 and 4, where k_{obs} is the measured rate constant for the exponential decay during phase 2 and f(RSH,NO) is a function of [RSH], [NO], and pH that defines the relationship between [**C**] and the limiting reagent $[Fe(II)]_{tot}$ (see SI Scheme S1).

$$Fe^{2+} + NO \underset{k_{-1}}{\overset{k_1}{\rightleftharpoons}} Fe(NO)^{2+}_{(aq)} \ (\mathbf{A}) \qquad (2)$$

$$\mathbf{A} + RSH \underset{k_{-2}}{\overset{k_2}{\rightleftharpoons}} Fe(NO)(RS)^{+}_{(aq)} \ (\mathbf{B}) + H^+ \qquad (5)$$

$$\mathbf{B} + RSH \underset{k_{-3}}{\overset{k_3}{\rightleftharpoons}} Fe(NO)(RS)_{2(aq)} \ (\mathbf{C}) + H^+ \qquad (6)$$

$$\mathbf{C} \xrightarrow{k_{rl}} \text{Products (P)} \qquad (3)$$

$$d[\mathbf{P}]/dt = d[\mathbf{C}]/dt = k_{rl}[\mathbf{C}] = k_{rl} \times f(RSH,NO)\,[Fe(II)]_{tot} = k_{obs}[Fe(II)]_{tot} \qquad (4)$$

Table 1 summarizes the k_{obs} values determined for phase 2 at different values of $[GSH]_{tot}$ (1.8-15 mM) using DynaFit kinetics software.[40,41] In each case, good exponential fits were obtained (e.g., SI Fig. S3). Since the pre-equilibria of phase 1 are established quickly relative to the much slower reaction of phase 2, k_{obs} represents the first-order rate constant for the conversion of ferrous iron (in all forms) to the products. The k_{obs} values are similar, although k_{obs} tends to be somewhat larger at the higher GSH concentrations. This behavior is attributed to the dependence of [**C**] on [GSH] (eq. 4) described in algebraic detail in SI Scheme S1. Thus, k_{obs} should approach k_{rl} at the higher values of $[GSH]_{tot}$ and $[NO]_{tot}$.

Table 1 also lists apparent product extinction coefficients (ε_{P350}(app)) calculated by dividing the absorbance of the final product at 350 nm by $[Fe]_{tot}$. This also changes with $[GSH]_{tot}$, as would be expected given that the equilibrium between the DNIC and RSE products is dependent on the thiol concentration (eq. 1).

A linear Eyring plot (SI Fig. S6) of k_{obs} values determined as a function of temperature (T = –5 to 25 °C) for the phase 2 reaction with $[Fe]_{tot}$ = 0.09 mM, $[NO]_{tot}$ = 0.93 mM, $[GSH]_{tot}$ = 1.8 mM gave the activation parameter values $\Delta H^{\ddagger}$ = 56 ± 3 kJ mol^{-1} and $\Delta S^{\ddagger}$ = −61 ± 5 J K^{-1} mol^{-1}. Although a positive $\Delta S^{\ddagger}$ might be expected for the unimolecular dissociation of **C**, the scenario illustrated in Scheme 1 is more intricate, given that **C** is assembled from GSH, NO and Fe(II) via several temperature dependent equilibria.

Table 1. Summary of observed rate constants (k_{obs}) and apparent product extinction coefficients (ε_{P350}) obtained from exponential fits of the phase 2 (temporal absorption curves at 350 nm) at different $[GSH]_{tot}$ ($[NO]_{tot}$ = 0.93 mM; $[Fe]_{tol}$ = 0.090 mM; pH 7.4 HEPES buffer; T = 298 K)[a]

$[GSH]_{tot}$ (mM)	k_{obs} (s^{-1})	ε_{P350}(app)[b] (10^3 M^{-1} cm^{-1})
1.8	0.83	5.01
2.7	0.85	5.02
3.6	0.84	5.05
5.4	0.88	5.02
7.5	0.82	5.05
10.0	0.90	4.97
15.0	0.92	4.88

[a] R^2 value is 0.999 for all fittings; [b]Absorbance of product solution divided by $[Fe]_{tot}$

The early spectral changes seen in Figure 2 provide the opportunity to analyze the fast phase 1 reactions leading to formation of **C** during the first 100 ms. Figure 3 illustrates the effects of varying GSH concentration on the temporal absorbance at 350 nm (Abs_{350}) while holding $[Fe(II)]_{tot}$ and $[NO]_{tot}$ fixed at 0.09 and 0.93 mM, respectively. Also shown is the concentration effect on the maximum absorbance ΔAbs_{350}(max) achieved during this phase, and it is notable that, at higher [GSH], ΔAbs_{350}(max) becomes essentially concentration independent. Similar temporal plots of Abs_{350} for different NO concentrations (0.28-0.93 mM) with fixed $[Fe(II)]_{tot}$ and [GSH] and for two different $[Fe(II)]_{tot}$ with fixed $[NO]_{tot}$ and [GSH] are shown in SI Figure S7. Again, it is observed that the reaction rate increases with increasing [NO] (SI Fig. S7) and that ΔAbs_{350}(max) levels off at higher concentration (SI Fig. S8). These observations are consistent with a series of pre-equilibria such as described by eq. 2 plus eqs. 5 and 6, leading to the formation of **C** with Fe(II) being the limiting reactant. Not surprisingly, the temporal absorbance changes at 350 nm do not correspond to single exponential functions.

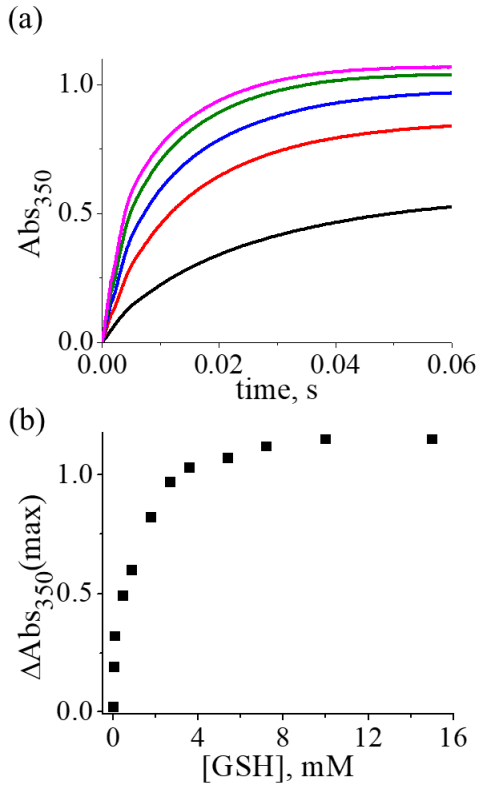

Figure 3. (a) Plots of Abs_{350} vs t for the phase 1 reactions of a solution prepared by stopped-flow mixing with final concentrations $[Fe]_{tot}$ = 0.090 mM, $[NO]_{tot}$ = 0.93 mM and various $[GSH]_{tot}$ (0.90 to 5.40 mM) in pH 7.4 HEPES buffer solution (200 mM) at 298 K. (b) Plot of ΔAbs_{350}(max) values during phase 1 vs [GSH] under these conditions.

When the phase 1 absorbance changes were monitored at 415 nm, the effects of changing $[GSH]_{tot}$ on the temporal Abs_{415} and on ΔAbs_{415}(max) (SI Fig. S9) were qualitatively similar. However, this value was achieved at a lower $[GSH]_{tot}$ than was ΔAbs_{350}(max), indicating that the process monitored at 415 nm is not identical to that monitored at 350 nm. As noted above, the isosbestic point at 415 nm in the latter stages of phase 1 indicates that sequential reactions are taking place. Since Abs_{415} reaches a plateau faster than does Abs_{350}, the former must sample a smaller number of initial steps than the latter. In other words, the dynamics of subsequent processes during phase 1 are not observed at 415 nm owing to its isosbestic nature. Therefore, we initiated a kinetics simulation using DynaFit kinetics software based on the temporal Abs_{415} data and a two-step sequential pre-equilibrium reaction model based on eqs. 2 and 5 (Model I).

In these simulations, the published values of k_1, k_{-1} for eq. 2 (1.24 $\times 10^6$ M^{-1} s^{-1}, 3.24 $\times 10^3$ s^{-1}, respectively) and ε_{A415} for **A** (230 M^{-1} cm^{-1})[38] were used. The molar extinction coefficient (ε_{B415}) for the isosbestic point at 415 nm (4.33 × 10^3 M^{-1} cm^{-1}) was estimated from the ΔAbs_{415}(max) plateau in SI Figure S9 by assuming **B** to be a mono-iron complex. The rate constants k_2 and k_{-2} were allowed to float in order to obtain an optimal fit. Table 2 summarizes the computed values of k_2 and k_{-2} that gave good fits for the temporal Abs_{415} curves in phase 1 for GSH concentration ranging from 1.8 to 15.0 mM. An alternative model in which the eq. 5 was treated as irreversible was tested but did not fit well to the kinetics data at 415 nm.

Table 2. Rate constants from fitting of Model I to temporal Abs_{415} curves in phase 1 for GSH[a,b]

Model I:	Fe^{2+} + NO ⇌ **A** (k_1, k_{-1}) **A** + RSH ⇌ **B** + H^+ (k_2, k_{-2})			
[GSH] mM	k_2 (10^5 $M^{-1}s^{-1}$)	k_{-2} (s^{-1})	$K_2 = k_2 / k_{-2}$ (10^4 M^{-1})	R^2
2.7	2.78	36.6	0.75	0.988
3.6	3.00	36.9	0.81	0.995
4.5	3.16	51.5	0.61	0.998
5.4	3.36	56.2	0.60	0.998
7.5	3.53	43.1	0.82	0.997
10.0	3.70	39.9	0.93	0.994
15.0	3.84	47.3	0.81	0.993
	3.34[c]	44.5[c]	0.76[c]	

[a] The values of k_1 = 1.42 × 10^6 M^{-1} s^{-1}, k_{-1} = 3.24 × 10^3 s^{-1}, ε_{A415} = 230 M^{-1} cm^{-1} and ε_{B415} = 4.55 × 10^3 M^{-1} cm^{-1} were fixed. [b] $[NO]_{tot}$ = 0.93 mM, T = 298 K. [c] ave. values

Next, the average values of k_2 and k_{-2}, obtained from fitting the temporal Abs_{415} curves in the two-step sequential reaction model (Table 2) were used in DynaFit simulations of phase 1 temporal Abs_{350} curves to the same model. However, as expected, these fits were poor; since it is obvious from Figure 2 that changes at Abs_{350} reflect at least one more step. Thus, a third reversible reaction involving a second GSH (eq. 6) was added (Model II). The ΔAbs_{350}(max) plateau in Figure 3b was used to calculate the extinction coefficient ε_{C350} = 12.8 × 10^3 M^{-1} cm^{-1} for **C** at 350 nm, also assuming **C** to be a mono-iron complex. However, the extinction coefficient for **B** (ε_{B350}) is unknown. Therefore, data from experiments where ΔAbs_{350}(max) has plateaued (7.5 to 15 mM GSH) were first used to fit the three-step model (Model II) in order to estimate ε_{B350} as 7.03 × 10^3 M^{-1} cm^{-1}.[42] Then, this estimated value was applied in the larger data set to simulate the temporal absorbance changes at 350 nm (SI Fig. S10). These curves fitted well to Model II. Table 3 presents these computational results using fixed values for k_1, k_{-1}, k_2, k_{-2}, ε_{A350}, ε_{B350} and ε_{C350} and by allowing k_3 and k_{-3} to float in order to obtain optimal fit.

In summary, the formation of dinitrosyl iron complexes from NO, Fe(II) and GSH in aqueous solution occurs via two phases, the first being quite fast with rates strongly dependent on the

concentrations of the three species. Although we have interpreted these rates in terms of three consecutive equilibria (eqs. 2, 5 and 6) it is likely that other sequences, such as the reaction of a Fe^{II}(GS) complex with NO, may also play a role in leading to species **C**. Thus, the observed kinetics represent a composite of reversible pathways, all of which are relatively fast. The much slower second stage is first order in the limiting reactant, $[Fe(II)]_{tot}$, consistent with the proposal that this reaction reflects the unimolecular autoreduction of $Fe^{II}(NO)(GS)_2$ (Scheme 1).

Table 3. Rate constants obtained from fits of Model II to the phase 1 of Abs_{350} curves for GSH [a,b]

Model II: $Fe^{2+} + NO \rightleftharpoons$ **A** (k_1, k_{-1})

A + RSH $\rightleftharpoons$ **B** + H^+ (k_2, k_{-2})

B + RSH $\rightleftharpoons$ **C** + H^+ (k_3, k_{-3})

[GSH] mM	k_3 (10^4 M^{-1} s^{-1})	k_{-3} (s^{-1})	K_3 (10^3 M^{-1})	R^2
1.8	1.90	15.3	1.24	0.994
2.7	1.93	14.6	1.32	0.997
3.6	2.08	10.8	1.93	0.999
5.4	1.36	9.35	1.45	0.997
	1.82[c]	12.5[c]	1.49[c]	

[a] The values of $k_1 = 1.42 \times 10^6$ M^{-1} s^{-1}, $k_{-1} = 3.24 \times 10^3$ s^{-1}, $k_2 = 3.34 \times 10^5$ M^{-1} s^{-1}, $k_{-2} = 44.5$ s^{-1}, $\varepsilon_{A350} = 3.7 \times 10^2$ M^{-1} cm^{-1}, $\varepsilon_{B350} = 7.03 \times 10^3$ M^{-1} cm^{-1}, $\varepsilon_{C350} = 1.28 \times 10^4$ M^{-1} cm^{-1} were fixed while k_3, k_{-3} were allowed to float. The ε_{B350} value was estimated from fits of the three-step model to phase 1 temporal absorption curves at 350 nm for experiments where $\Delta Abs_{350}(max)$ has plateaued at higher $[GSH]_{tot}$; [b] $[NO]_{tot} = 0.93$ mM, T = 298 K. [c] ave. values.

Dinitrosyl iron complex formation with CysSH

The stopped-flow mixing of CysSH, Fe(II) and NO in aqueous buffer pH 7.4 led to well-defined phase 1 and 2 as observed previously[25] and for the analogous reaction with GSH, although the temporal absorption spectra after mixing did not present an isosbestic point at 415 nm (SI Fig S11). In addition, the plot of $\Delta Abs_{350}(max)$ vs [CysSH] for phase 1 reached a plateau at a [CysSH] much lower than with GSH (SI Fig. S12). This last observation is consistent with CysSH having a lower pKa (8.2 ± 0.2) than GSH (9.4 ± 0.2),[43] thereby making reactions such as eq. 5 and 6 more favorable.

In the absence of the 415 nm isosbestic point in phase 1, the three-step sequential reaction model (Model II) was directly used to fit the phase 1 of the 350 nm curves (SI Tables 1-2). From these fits were obtained the average values $k_2 = 4.9 \times 10^5$ M^{-1} s^{-1}, $k_{-2} = 20$ s^{-1}, $k_3 = 2.2 \times 10^4$ M^{-1} s^{-1} and $k_{-3} = 3.4$ s^{-1}. The exponential decay of phase 2 displayed a modest sensitivity to $[CysSH]_{tot}$ and $[NO]_{tot}$ as expected from eq. 4 and gave a limiting k_{obs} value of ~3.6 s^{-1} at the highest CysSH concentration (3.6 mM). This k_{rl} value is within the experimental uncertainty of that determined previously (4.0 ± 0.5 s^{-1}) [25] under very similar conditions and is 4-fold higher than that obtained for GSH.

Reactions with WCGPC or WCGPY

Owing to the similarity of its motif to the active site of certain redox enzymes, WCGPC was chosen as a substrate, while WCGPY was chosen to evaluate the influence of a nearby tyrosine on DNIC formation. The patterns of temporal optical spectral changes after stopped-flow mixing of buffered solutions of Fe(II), NO and WCGPC or WCGPY (Fig. 4 and SI Fig. S13, respectively) proved to be similar, but not identical to that observed for GSH and CysSH. Two stages were again observed, phase 1 occurring over approximately 100 ms and giving a marked absorbance increase at ~350 nm; and phase 2 involving an exponential Abs_{350} decrease over the following seconds. The eventual spectrum was consistent with formation of a RSE/DNIC mixture, but did not give bands as distinctive for RSE at low [RSH] or for DNIC at higher [RSH] as seen with GSH or CysSH (SI Fig. S1), owing to the overlap of the peptide with the product spectra at short wavelengths. Nonetheless, the EPR spectra of the products clearly display characteristic g = 2.03 EPR signals corresponding to DNIC formation (see below).

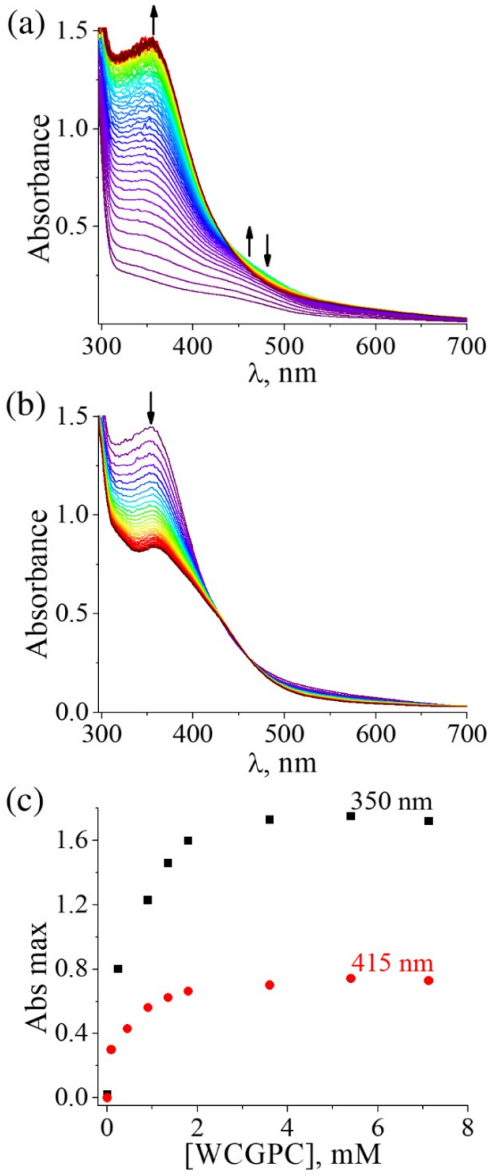

Figure 4. (a) Temporal absorption spectra from 2 to 100 ms after stopped-flow mixing of Fe(II) (0.09 mM), NO (0.93 mM) and WCGPC (1.35 mM) (phase 1). (b) Temporal spectra from 100 ms to 3 s (phase 2) for the same solution. (c) Concentration dependence of $\Delta Abs_{415}(max)$ and $\Delta Abs_{350}(max)$ for reaction over the [WCGPC] range 0.27-7.1 mM in pH 7.4 aqueous buffer (298 K).

For WCGPC, the phase 2 k_{obs} values were dependent on peptide concentration as predicted by eq. 4 and gave a nearly limiting value of ~1.9 s^{-1} at the highest concentration studied (SI Table S3). This k_{II} value is about 2-fold higher than that seen for GSH (~0.9 s^{-1}) under comparable conditions.

The phase 1 spectral changes for WCGPC (Fig. 4a) displayed the early rise and fall of absorbance at ~450 nm and a developing isosbestic point at 415 nm as seen with GSH. Furthermore, values of both $\Delta Abs_{415}(max)$ and $\Delta Abs_{350}(max)$ (Fig. 4c) proved to be dependent on the WCGPC concentration over the range 0.27 to 1.80 mM but reached limiting values at the higher [WCGPC] tested. Given these strong similarities, the kinetics model employed for GSH was used to fit the temporal absorption curves for the phase 1 reactions with WCGPC (SI Tables 4 & 5). This analysis gave the average rate constants k_2 = 3.1 × 10^5 M^{-1} s^{-1}, k_{-2} = 21 s^{-1}, k_3 = 3.5 × 10^4 M^{-1} s^{-1} and k_{-3} = 20 s^{-1}.

The analogous reactions with WCGPY presented the two-stage pattern quite consistent with those seen for each of the thiols described before (SI Fig. S13). Notably, the plot of $\Delta Abs_{350}(max)$ vs [WCPGY] for phase 1 required a higher thiol concentration (~8-10 mM) to reach a plateau (Fig. 5) than with GSH, CysSH or WCGPC. The k_{obs} values for phase 2 decay displayed a modest dependence on [WCPGY] (SI Table 6), giving a k_{obs} for 7.1 mM WCPGY (~1.8 s^{-1} at 298 K) similar to that for WCGPC.

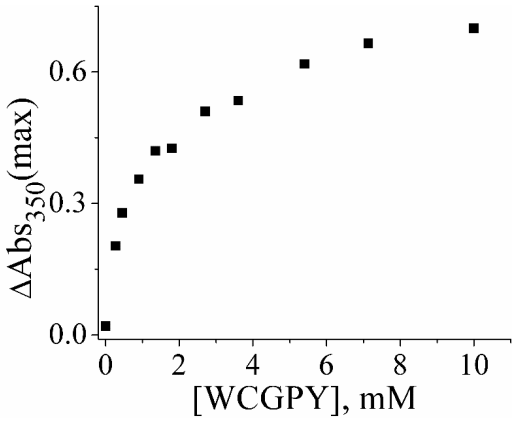

Figure 5. Maximum absorption at 350 nm during phase I after stopped-flow mixing of Fe(II) (0.090 mM), NO (0.93 mM) and WCGPY peptide (0.09-10 mM) in pH 7.4 solution, T = 298 K.

Like CysSH, the temporal absorption spectra during phase 1 for WCGPY did not present an isosbestic point at 415 nm (SI Fig. S12). Therefore, a kinetics model analogous to that used for CysSH was used to fit temporal absorption curves for phase 1 reactions with WCGPY. The ε_{B350} value was estimated as 4.75 × 10^3 $M^{-1}cm^{-1}$ from fits of the three-step model to phase 1 temporal absorption curves at 350 nm for higher $[WCGPY]_{tot}$ where $\Delta Abs_{350}(max)$ has nearly plateaued. The same experiments gave an estimated value for ε_{C350} (7.9 × 10^3 $M^{-1}cm^{-1}$). Fits of temporal absorption curves at 350 nm to Model II gave the averaged rate constants k_2 = 6.0 × 10^5 M^{-1} s^{-1}, k_{-2} = 5 × 10^2 s^{-1}, k_3 = 2.6 × 10^4 M^{-1} s^{-1} and k_{-3} = 17 s^{-1} (SI Table 7); however, there was considerable uncertainty in these values.

We further examined whether tyrosine might promote reduction of Fe(II) under these conditions by stopped-flow mixing a pH 7.4 aqueous solution of Fe(II) (0.09 mM), NO (0.93 mM) and tyrosine (1.8 mM). The presence of Fe(II) and NO led to weak absorbances at 345 and 440 nm (SI Fig. S14) similar to those seen for $Fe(NO)^{2+}_{(aq)}$ (SI Fig. S3), but no further reaction was apparent even up to 5 min after mixing. More convincingly, the ambient temperature EPR spectrum of a solution consisting of Fe(II) (0.09

mM), NO (0.93 mM) and tyrosine (1.8 mM) showed no signal at g = 2.03, indicating that this mixture does not spontaneously form a tyrosine based DNIC.

Thus, WCGPC and WCGPY demonstrate the two phase reaction pattern, proceeding through formation of a species **C** followed by a much slower unimolecular decay to give the final products as observed for GSH and CysSH. Since the k_{rl} values for the rate-limiting unimolecular decay pathway are very similar, substituting a potentially redox-active tyrosine for the terminal cysteine in WCGPC had, at most, a modest effect on the dynamics of dinitrosyl iron complex formation. Apparently, the presence of two potentially chelating nearby residues in the peptide did not promote major changes in the reaction mechanism or dynamics of dinitrosyl iron complex formation.

EPR experiments: detection and quantification of DNIC

The reaction of Fe(II), NO and low molecular thiols in aqueous media leads to an equilibrium mixture of the mono-nuclear (DNIC) and bi-nuclear (RSE) dinitrosyl iron complexes (eq. 1). Although the absorption spectra of the RSEs (bands at λ_{max} = 310 and λ_{max} = 360 nm; shoulder at ~435 nm) are distinct from those of the corresponding DNIC (band at λ_{max} ~ 400 nm), quantitative analysis of the relative concentrations is problematic owing to band superposition. Therefore, we used EPR to quantify the paramagnetic DNIC in a product mixture prepared from reaction of $[Fe(II)]_{tot}$ = 0.09 mM, $[NO]_{tot}$ = 0.93 mM and $[RSH]_{tot}$ = 3.60 mM in deaerated HEPES buffer (200 mM) at pH 7.4. The limiting reactant is Fe(II), and it is fully converted into dinitrosyl iron complexes under these conditions. Figure 6 displays the resulting EPR spectra for these solutions. In each case, the derived EPR signal centered at g = 2.03 indicates the formation of the respective mono-nuclear DNIC complex. The concentrations of formed DNICs were obtained by double integration of the EPR spectra using the same baseline correction and comparison with the area of the spectrum of a known concentration of tempol.[42] These areas proved to be a function of the specific thiol with CysSH giving the highest and GSH the loweest concentration. Based on the assumption that the only other iron-containing product is the corresponding RSE, we used the relationship [RSE] = 0.5 ($[Fe]_{tot}$ –[DNIC]) to calculate [RSE]. The resulting values under these conditions are summarized in Table 4, but it should be noted that, given the stoichiometry of eq. 1, the [RSE]/[DNIC] ratio is a function of $[Fe]_{tot}$, $[RSH]_{tot}$ and pH, as well as a function of the nature and pKa of the specific thiol.

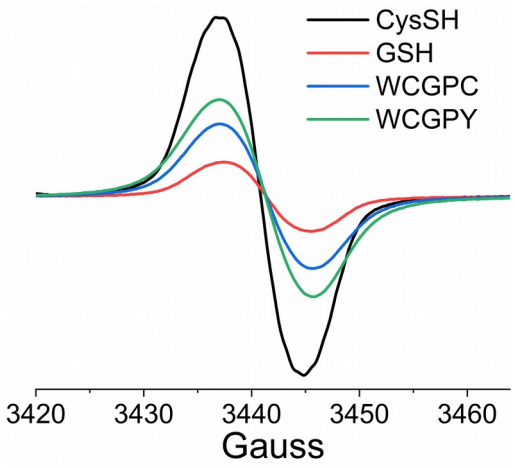

Figure 6. EPR spectra of a deaerated solution of Fe(II) (0.09 mM), NO (0.93 mM) and GSH (3.60 mM) (green line), CysSH (3.6 mM) (black line), WCGPC (3.60 mM) (red line) or WCGPY (3.60 mM) (blue line). HEPES buffer at pH 7.4 and T = 298 K. The signals are each centered at g = 2.03.

Table 4. Concentrations DNIC and RSE obtained from the tested thiols in aqueous medium pH 7.4 [a,b,c]

Thiol	DNIC[b] (μM)	RSE[c] (μM)	$K = [DNIC]^2/([RSE][RSH]^2)$ (M^{-1}) at pH 7.4
CysSH	48.3	20.9	9.3
GSH	10.0	40.0	0.2
WCGPC	23.5	33.3	1.4
WCGPY	33.8	28.1	3.3

[a] Solutions prepared from $[Fe(II)]_{tot}$ = 0.09 mM, [NO] = 0.93 mM and $[RSH]_{tot}$ = 3.60 mM in deaerated HEPES buffer (200 mM) at pH 7.4 and T = 298 K. [b] DNIC concentration was quantified by EPR using known concentration of tempol solutions as standard. [c] RSE concentration was calculated assuming the full conversion of Fe(II) into DNIC and RSE species.

Density functional theory (DFT) computations:

The above kinetics data for the first phase was interpreted in terms of three sequential reversible steps (eqs. 2, 5 and 6) leading to the Fe(II) species **A**, **B** and **C** (Model II in Table 3). The rate-limiting step giving the dinitrosyl iron complex products (DNIC and RSE) was further interpreted as the unimolecular autoreduction of **C** (Scheme 1) that was accompanied by formation of mono-nitrosyl iron complex(es) plus thiyl radicals ($RS^{\bullet}$) as shown by EPR experiments (eq. 7). In order to gain greater insight into structures, energies and spectra of the proposed intermediates, DFT and time-dependent DFT (TDDFT) studies were carried out at the UB3LYP/DGDZVP level of theory in water (PCM approach) using the computational packages of Gaussian 16.

The calculations were carried out for RSH = CysSH, which was the simplest thiol studied, and the overall behavior of which was analogous to that of GSH, WCGPC or WCGPY. SI Table S8 summarizes the calculated energies for the key species.

Although formation of **A** from $Fe^{2+}_{(aq)}$ and NO is too fast to monitor with the stopped-flow technique, this technique was able to monitor the sequential processes leading to **B** and **C**. The TDDFT calculated spectra for species **A** and **B** are shown in SI Figure S15. The former displays two weak, visible range bands consistent with the spectrum for the known complex[38] $Fe(H_2O)_5(NO)^{2+}$ (reported above), although the calculated band energies are about 0.32 and 0.68 eV lower energy than the experimental values (differences up to 1 eV are considered reasonable fits). While the highest occupied molecular orbitals (HOMOs) and the lowest unoccupied molecular orbitals (LUMOs) are of mixed character, the overall patterns suggest that these bands essentially represent metal (Fe) to nitrosyl (NO) transitions.

The calculated spectrum for **B** is markedly different. The predicted absorption bands at 297 and 346 nm are quite strong, and a broad absorption at ~400-450 nm is present. Based on the HOMO to LUMO transitions (SI Figure S16), the strong band at ~350 nm can be considered to be a mixture of ligand (thiolate)-to-metal charge transfer (LMCT) and ligand to ligand' (nitrosyl) charge transfer (LL'CT) transitions. Qualitatively, the calculated spectrum of **B** is consistent with the temporal changes in the absorption spectra observed immediately upon mixing Fe^{2+}, RSH and NO in the stopped-flow experiments and attributed to the conversion of **A** to **B** (eq. 5).

SI Figure S17 displays the calculated electronic spectra and formulated structures for species **C** that differ in the number of coordinated waters: $Fe^{II}(NO)(CysS)_2(H_2O)$ (C-1), $Fe^{II}(NO)(CysS)_2(H_2O)_2$ (C-2), $Fe^{II}(NO)(CysS)_2(H_2O)_3$ (C-3). All three show very strong bands in the 300-400 nm wavelength range, with the C-1 spectrum being the most consistent with the experimental spectrum of **C**. As illustrated for C-1 (SI Fig. S18), the difference in the electronic distributions between the HOMO and the LUMOs indicate that these absorption bands are also best represented as LL'CT transitions. Calculation of the equilibria between these species in aqueous solution (see SI Table S9) also shows C-1 to be modestly the most stable, with C-2 and C-3 being 13 and 23 kJ mol^{-1} higher energy, respectively. Notably, the calculated structures of C-1 and C-2 are both 5-coordinate, with the carboxylate of a zwitterionic cysteine carboxylate occupying one of the coordination sites in the former. The lowest energy form of C-3 was not 6-coordinate, but appeared to be C-2 with a loosely associated H_2O; the 6-coordinate structure in SI Figure S16 represents a local minimum 27 kJ mol^{-1} higher energy than the value listed SI Table S8.

Scheme 2. Auto-reduction of C-1, C-2 and C-3 in aq. solution.

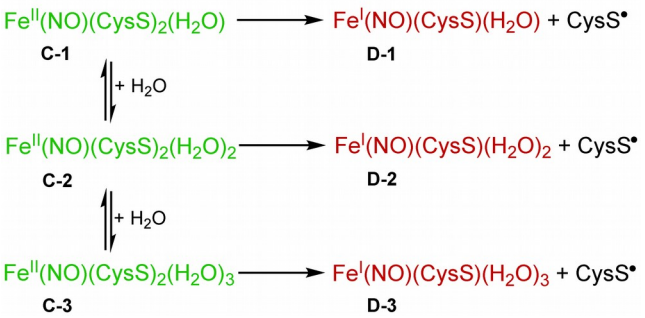

The question remains regarding which formulation of C might be responsible for the auto reduction depicted in eq. 7. SI Table S9 summarizes the calculated energetics of this process for C-1, C-2 and C-3 as depicted in Scheme 2. The calculated ΔE for the C-1 → D-1 + CysS• reaction is 121 kJ mol^{-1} while that for C-2 → D-2 + CysS• is significantly lower at 72 kJ mol^{-1}. The ΔE for C-3 → D-2 + CysS• + H_2O is very similar (62 kJ mol^{-1}) as expected given that C-3 converges to the lowest energy structure, close to that of C-2. The latter two ΔE values compare favorably to the value of +59 kJ mol^{-1} from an earlier DFT calculation for this reaction in a dielectric continuum using the same level of theory but a different software package, Gaussian 09.[25] The direct reaction of C-3 to D-3 + CysS• has a more positive ΔE (+98 kJ mol^{-1}). Thus, if we assume that the principal form of **C** is C-1, then the lowest energy pathway corresponding to eq. 7 would be reaction with H_2O to form C-2 (ΔE = +13 kJ mol^{-1}) followed by auto reduction to give D-2 (ΔE = +72 kJ mol^{-1}) as illustrated in Scheme 3. Although this calculated pathway would be endoergic (ΔE_{total} = +85 kJ mol^{-1}), the subsequent reactions of the initial intermediates formed are sufficiently exoergic to provide a strong driving force for the overall process. For comparison, the experimentally determined $\Delta H^{\ddagger}$ reported here for the analogous reaction with GSH was 56 ± 3 kJ mol^{-1}, and one might speculate that the negative entropy of activation ($\Delta S^{\ddagger}$ = −61 ± 5 J K^{-1} mol^{-1}) observed may partially reflect the C-1 reaction with H_2O to give C-2.

Scheme 3. DFT calculated energies showing that the lowest energy autoreduction path is via C-2.

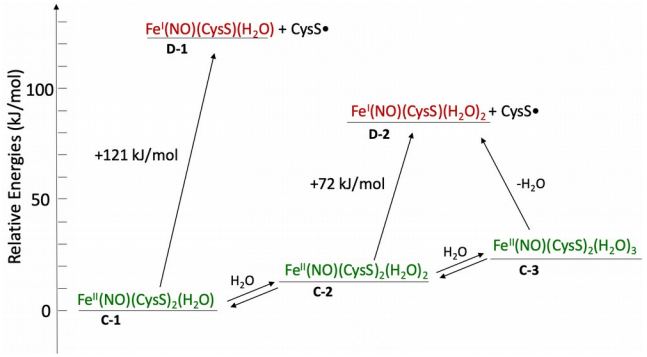

DISCUSSION

NO reacts with the intracellular chelatable iron pool to form dinitrosyl iron complexes[12,15] most of which are protein-bound, although low molecular weights DNICs may play key role in transporting iron out of cells.[29] In this work, we focused on the kinetics and mechanism of the formation of DNICs from several low molecular weight biothiols, Fe(II) and NO at pH 7.4. The employed NO concentrations are much higher than those found in living organisms, however, the rate constants determined here are applicable to biological conditions, demonstrating the facile DNIC formation under these conditions.

DNIC formation proceeds via two phases. The first, occurring in a few tens of milliseconds represented as the facile substitution reactions of aqueous divalent iron to give a mono-nitrosyl iron(II) complex coordinated to two thiols (or thiolates), i.e. the intermediate Fe^{II}(NO)(RS)$_2$ (**C** in Scheme 1**)**. The somewhat slower phase 2, with a lifetime of seconds, is the unimolecular decay of the latter to give an equilibrium mixture of mono- and bi-nuclear dinitrosyl iron complexes.

Kinetics simulations provided pertinent rate constant values from temporal changes in the optical absorption spectra. Each of the biothiols studied (CysSH, GSH, WCGPC and WCGPY) exhibited very rapid formation of the iron(II) intermediate Fe^{II}(NO)(RS)$_2$ (**C**). The equilibrium constants calculated by simulation for the proposed sequential reversible substitutions reactions of phase 1 (Model II) are listed in Table 5. Given the lability of Fe^{2+}(aq),[43] any kinetics model is simplistic, although the overall equilibria forming the key intermediates are relevant regardless of the specific sequence of ligand substitution reactions. In this context, the product of the three equilibrium constants (K_1, K_2 and K_3) should be equal to the overall equilibrium constant for the formation of the intermediate **C** at pH 7.4. The value of the latter product can be estimated from K_C = [**C**]/([Fe^{2+}][NO][RSH]^2), since [**C**] can be calculated using the extinction coefficient ε_{C350} determined at limiting RSH concentrations during the phase 1 reactions for each thiol. Similarly, for GSH and WCGPC, which presented the isosbestic point at 415 nm, the K_B can also be calculated (K_B = [**B**]/([Fe^{2+}][NO][RSH]); [**B**] = Abs$_{415}$(max)/ε_{B415}). Considering the inherent uncertainties in rate constants determined by kinetic simulations, the values of K_B and K_C calculated from the products K_1K_2 and $K_1K_2K_3$, respectively, are surprisingly close to the K_B and K_C values calculated from the concentrations of **B** (Fe^{II}(NO)(RS)) or **C** (Fe^{II}(NO)(RS)$_2$) and of the other reactants (Table 5). Thus, the kinetic model proposed here is internally self-consistent.

For each biothiol studied, the Fe(II) was shown to be fully converted into dinitrosyl iron complexes at sufficiently high concentrations of NO and thiol. The fastest reactions were seen with cysteine, and while this might be attributed to its smaller size relative to the polypeptide thiols, the lower pKa of CysSH is also a likely reason for this behavior as well as for the significantly higher DNIC]/[RSE] ratio for CysSH compared to GSH. If one compares WCGPC and WCGPY, the first step in DNIC assembly is the reversible formation of the proposed intermediate **B**, which is about an order of magnitude more favorable for WCGPC owing perhaps to the presence of a second thiol. The difference in this first step is further reflected in the formation constant for species **C**, but there is little limiting rate difference in the decay of **C** to the dinitrosyl iron complexes. Overall the influences of the other peptide residues on the dynamics of DNIC formation are relatively subtle and may be due to different, possibly competing, effects. Further investigations are needed in order better elucidate such issues that are surely relevant to the formation of protein DNICs

The obtained rate constants (Table 5) were applied to simulate DNIC formation under biological conditions. The rate of NO production per cell in activated macrophages (2.8 μM s^{-1}) was used to simulate inflammatory conditions,[44,45] whereas 1% of the latter flux (28 nM s^{-1}) was used to simulate non-inflammatory conditions.[45] Considering the variable levels determined for the cellular chelatable iron pool (0.1 to 10 μM),[46] we used the Fe(II) concentration of 5 μM and the upper limit of intracellular GSH (10 mM) or CysSH (1 mM) concentrations (Fig. 7). As expected, the simulations showed that NO fluxes modulate the rate of DNIC formation. Under inflammatory conditions, the Fe(II) would be fully converted into DNICs within 10-15 s at intracellular levels of GSH or CysSH. Notably, although the intracellular concentration of CysSH is an order of magnitude lower than that of GSH, the higher reactivity makes CysSH biologically relevant for DNIC formation. Under non-inflammatory conditions, DNIC formation would be much slower but about 95 % of total NO produced incorporates into DNICs within 30 s. These calculations are in line with quantitative studies using macrophage cell lines, indicating that DNICs are the most abundant NO-adduct formed in all cellular settings of NO production.[15] It should be noted that our kinetic studies were performed at 298 K and more rapid rates are expected at physiological temperatures.

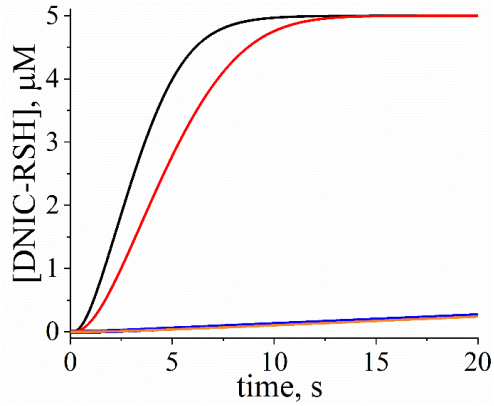

Figure 7. Time course simulations using Gepasi software for formation of DNICs from Fe(II) (5 μM) under biologically relevant concentrations showing the effects of different RSH concentrations and NO fluxes. The rate constants used are listed in Table 5 for reactions in pH 7.4 aqueous buffer solution at 298 K. Black line: [GSH] = 10 mM, NO flux 2.8 μM s^{-1}. Red : [CysSH] = 1 mM, NO flux 2.8 μM s^{-1}. Blue: [GSH] = 10 mM, NO flux 28 nM s^{-1}. Orange: [CysSH] = 1 mM, NO flux 28 nM s^{-1}

Table 5. Summary of equilibrium constants for reactions that lead to DNIC formation from reaction of Fe(II), NO and various thiols in pH 7.4 aqueous buffer solution at 298 K.

RSH	$K_2 = k_2/k_{-2}$ (10^3 M^{-1})[a]	K_1K_2 (10^6 M^{-2})[b]	K_B (10^6 M^{-2})[c]	$K_3 = k_3/k_{-3}$ (10^3 M^{-1})[a]	$K_1K_2K_3$ (10^9 M^{-3})[b]	K_C (10^9 M^{-3})[d]	k_{rl} (s^{-1})
CysSH	25.	10.4	-	2.6	29.	21.	3.6
GSH	7.5	3.1	2.4	1.5	4.8	1.3	0.92
WCGPC	14.6	6.1	5.0	1.7	11.	4.5	1.92
WCGPY	1.19	0.50	-	1.5	0.80	0.51	1.81

[a] The values of equilibrium constants K_2 and K_3 correspond to the average of the values obtained from the fits of the kinetic model to the temporal absorption curves using Dynafit [b] $K_1 = k_1/k_{-1}$ (k_1 = 1.42 × 10^6 M^{-1} s^{-1} and k_{-1} = 3.24 × 10^3 s^{-1})[38]. [c] Calculated using K_B = [**B**]/([Fe^{2+}][NO][RSH]). The concentration of **B** was obtained using [B] = Abs_{415}(max)/ε_{B415}. [d] Calculated using K_C = [**C**]/([Fe^{2+}][NO][RSH]^2). The concentration of **C** was obtained using [**C**] = Abs_{350}(max)/ε_{C350}. The K_B and K_C were obtained at different RSH concentrations and then average

Our results also demonstrate that the rate constants for the autoreduction of **C** and, consequently, the rates of DNIC formation are function of biothiol nature with k_{rl} following the order CysSH > WCGPC > WCGPY > GSH (Table 5). Relevantly, the autoreduction of **C** generates thiyl radicals which in a NO rich environment will result in S-nitroso thiol formation. The S-nitroso thiols have gained attention owing to possible involvement in NO-signaling under physiological and pathological conditions.[47,48] However, the mechanisms of RSNO formation in biological medium remain debatable. Our studies showing the concomitant production of DNICs and thiyl radicals[33] provide a novel route for RSNO formation *in vivo.*

Conclusion:

In summary, we have demonstrated the dynamics for the overall assembly (phase 1 and 2) of several low molecular weight DNICs from the direct reaction among NO, Fe(II) and biothiols in pH 7.4 aqueous media. The first phase involves a series of reversible equilibria to produce the intermediate $Fe^{II}(NO)(RS)_2$. The second phase is the rate-limiting unimolecular decay of $Fe^{II}(NO)(RS)_2$ via auto reduction accompanied by formation of thiyl radicals and mononitrosyl iron(I) complex, which is rapidly converted to the respective DNIC and RSE. Modeling with the determined rate constants and biological concentrations of the reactants confirm that DNICs are readily formed at physiological and pathological levels of NO production.

EXPERIMENTAL SECTION

Materials and Methods

The reagents L-glutathione (reduced) (≥ 98.0%), L-cysteine (≥ 98.0%) and iron(II) sulfate heptahydrate (> 99.0%) were purchased from Sigma Aldrich. The peptides WCGPC and WCGPY were purchased from Biomatik. Solutions at pH 7.4 were prepared with HEPES buffer (≥ 99.5%), while those at pH 8.6 and 9.0 were prepared in TRIS buffer (≥ 99.0%).

Nitric oxide gas purification and solution preparation.

Nitric oxide gas (99.5%) from the tank (PraxAir) was passed through a stainless-steel column containing sodium hydroxide pellets to remove NO_2 and N_2O_3. The sodium hydroxide pellets were crushed and dried under vacuum before being packed into the column. In order to obtain solutions containing the desired NO concentration, the buffered solutions were deoxygenated in Schlenk flasks using the freeze-pump-thaw method. Then,

NO gas was introduced to the headspace of the Schlenk flask on a vacuum line. The samples were allowed to equilibrate for a minimum of 40 min. The total pressure of the system was measured using a mercury manometer.[49] The NO concentration was calculated by the partition coefficient between the gas and the liquid phases (K_H = 1.86 mM/atm at 298 K).[50]

Stopped-flow measurements.

Kinetics studies were performed in an upgraded Applied Photophysics model SX-18 MV stopped-flow spectrophotometer with either a photomultiplier tube (PMT) or a photodiode array (PDA) used as the detector. Gas-tight syringes with on-off valves were used to transfer solutions from Schlenk flasks to the stopped-flow instrument. The transfer syringes were purged several times with argon prior to insertion into the sample flasks. The reservoir syringes on the stopped-flow were flushed with several volumes of the deoxygenated buffer solution before the introduction of the sample solution. The temperature control was performed by a thermostatic, circulating water bath. The symmetrical mixing operation mode was used in all experiments. In general, one of the syringes was loaded with NO saturated HEPES buffer (200 mM) solution at pH 7.4 ($[NO]_{tot}$ = 1.86 mM, 1 atm and 298 K) while the second syringe was loaded with degassed HEPES buffer (200 mM) solution at pH 7.4 containing ferrous sulfate ($[Fe(II)]_{tot}$ = 0.18 mM) and different concentrations of thiols. The stopped-flow kinetics data were processed using OriginPro software.

Simulations of the reaction mechanism on kinetics curves.

The kinetic simulations were performed with DynaFit software.[40,41] The absorbance vs. time data for the reactions between Fe(II), NO and thiols (RSH = cysteine, glutathione, CGPC peptide or WCGPY peptide) were used to fit the kinetics models described above. In each specific simulation, known values of rate constants and molar absorptivity coefficients were fixed while unknown ones were allowed to float. The R^2 was used as parameter to evaluate the goodness of fittings.

Time course simulations for DNIC formation were performed using Gepasi v3.30 (http://www.gepasi.org)[51] and taking into account the reactions shown in Scheme 1, the rate constants in Table 4, the initial concentrations of Fe(II) (5 μM), thiol (10 mM for glutathione or 1 mM for cysteine), and a constant NO flux (2.8 μM s^{-1} or 28 nM s^{-1}).

EPR Spectroscopy.

The static EPR spectra for direct detection of DNIC were acquired using a Bruker EMX spectrometer equipped with a high sensitivity cavity. The experiments were performed at room temperature using a flat cell. The EPR instrument operated at 9.85 GHz microwave frequency, 150 G range, 4 G amplitude modulation, 100 kHz frequency modulation, 163.84 ms time constant, microwave power of 20 mW and 2 scans. The EPR signal was quantified using a known concentration of tempol solutions as standard.[41]

Density Functional Theory Methods.

DFT calculations were performed with Gaussian 16 software package. The ground state structures were optimized at spin unrestricted B3LYP/DGDZVP level of theory without symmetry constraints, then the time-dependent DFT was used to obtain calculated UV-Vis spectra. All calculations in the ground and excited states were completed in the presence of a solvent (water) using Integral Equation Formalism of the Polarizable Continuum Model (IEFPCM).

ASSOCIATED CONTENT

Supporting Information

The Supporting Information is available free of charge via the Internet at http://pubs.acs.org/. This includes additional documentation (1 scheme, 9 tables, and 18 figures) of the studies described in this manuscript (24 pages total, PDF).

AUTHOR INFORMATION

Corresponding Authors

*E-mail: dtruzzi@iq.usp.br (DRT)
ford@chem.ucsb.edu (PCF)

ORCID

Daniela Ramos Truzzi: 0000-0003-4421-9621

Peter C. Ford: 0000-0002-5509-9912

Present Addresses

Daniela R. Truzzi: Departamento de Bioquímica, Instituto de Química de São Paulo, Universidade de São Paulo, Caixa Postal 26077, CEP05513-970, São Paulo, SP, Brazil

Funding Sources

This work was partially supported by a grant to PCF from US National Science Foundation (CHE-1565702). DRT acknowledges postdoctoral fellowship support from Fundação de Amparo à Pesquisa do Estado de São Paulo (FAPESP) Grants 2014/09518-5 and 2017/02728-2 OA acknowledges the financial support from FAPESP Grant 2013/07937-8. DRT and OA are members of the Research, Innovation and Dissemination Center (RIDC) Redoxoma (FAPESP). DFT calculations were accomplished on computational facilities purchased with funds from the National Science Foundation (CNS-1725797) and administered by the UC Santa Barbara Center for Scientific Computing (CSC). The CSC is supported by the California NanoSystems Institute and the UCSB Materials Research Science and Engineering Center (MRSEC; NSF DMR 1720256).

Notes

The authors declare no competing financial interests.

REFERENCES

(1) *Nitric Oxide: Biology and Pathobiology*, Third edition.; Ignarro, L. J., Freeman, B. A., Eds.; Academic Press, Elsevier: London, United Kingdom, 2017.

(2) Toledo, J. C., Jr; Augusto, O. Connecting the Chemical and Biological Properties of Nitric Oxide. *Chem. Res. Toxicol.* **2012**, *25* (5), 975–989.

(3) Heinrich, T. A.; da Silva, R. S.; Miranda, K. M.; Switzer, C. H.; Wink, D. A.; Fukuto, J. M. Biological Nitric Oxide Signalling: Chemistry and Terminology. *Br. J. Pharmacol.* **2013**, *169* (7), 1417–1429.

(4) Wink, D. A.; Mitchell, J. B. Chemical Biology of Nitric Oxide: Insights into Regulatory, Cytotoxic, and Cytoprotective Mechanisms of Nitric Oxide. *Free Radic. Biol. Med.* **1998**, *25* (4–5), 434–456.

(5) Ford, P.; Clayston Melo Pereira, J.; Miranda, K. Mechanisms of Nitric Oxide Reactions Mediated by Biologically Relevant Metal Centers. *Structure and Bonding*; **2013**; 154, 99–135.

(6) Goldstein, S.; Czapski, G. The Reaction of NO· with O2·− and HO2·−: A Pulse Radiolysis Study. *Free Radic. Biol. Med.* **1995**, *19* (4), 505–510.

(7) Madej, E.; Folkes, L. K.; Wardman, P.; Czapski, G.; Goldstein, S. Thiyl Radicals React with Nitric Oxide to Form S-Nitrosothiols with Rate Constants near the Diffusion-Controlled Limit. *Free Radic. Biol. Med.* **2008**, *44* (12), 2013–2018.

(8) Thomas, D. D.; Miranda, K. M.; Colton, C. A.; Citrin, D.; Espey, M. G.; Wink, D. A. Heme Proteins and Nitric Oxide (NO): The Neglected, Eloquent Chemistry in NO Redox Signaling and Regulation. *Antioxid. Redox Signal.* **2003**, *5* (3), 307–317.

(9) Ford, P. C. Reactions of NO and Nitrite with Heme Models and Proteins. *Inorg. Chem.* **2010**, *49* (14), 6226–6239.

(10) Lancaster, J. R.; Hibbs, J. B. EPR Demonstration of Iron-Nitrosyl Complex Formation by Cytotoxic Activated Macrophages. *Proc. Natl. Acad. Sci. U.S.A.* **1990**, *87* (3), 1223–1227.

(11) Stadler, J.; Bergonia, H. A.; Di Silvio, M.; Sweetland, M. A.; Billiar, T. R.; Simmons, R. L.; Lancaster, J. R. Nonheme Iron-Nitrosyl Complex Formation in Rat Hepatocytes: Detection by Electron Paramagnetic Resonance Spectroscopy. *Arch. Biochem. Biophys.* **1993**, *302* (1), 4–11.

(12) Toledo, J. C.; Bosworth, C. A.; Hennon, S. W.; Mahtani, H. A.; Bergonia, H. A.; Lancaster, J. R. Nitric Oxide-Induced Conversion of Cellular Chelatable Iron into Macromolecule-Bound Paramagnetic Dinitrosyliron Complexes. *J. Biol. Chem.* **2008**, *283* (43), 28926–28933.

(13) Crack, J. C.; Hamilton, C. J.; Brun, N. E. L. Mass Spectrometric Detection of Iron Nitrosyls, Sulfide Oxidation and Mycothiolation during Nitrosylation of the NO Sensor [4Fe–4S] NsrR. *Chem. Commun.* **2018**, *54* (47), 5992–5995.

(14) Ekanger, L. A.; Oyala, P. H.; Moradian, A.; Sweredoski, M. J.; Barton, J. K. Nitric Oxide Modulates Endonuclease III Redox Activity by a 800 MV Negative Shift upon [Fe4S4] Cluster Nitrosylation. *J. Am. Chem. Soc.* **2018**, *140* (37), 11800–11810.

(15) Hickok, J. R.; Sahni, S.; Shen, H.; Arvind, A.; Antoniou, C.; Fung, L. W. M.; Thomas, D. D. Dinitrosyliron Complexes Are the Most Abundant Nitric Oxide-Derived Cellular Adduct: Biological Parameters of Assembly and Disappearance. *Free Rad. Biol. Med.* **2011**, *51* (8), 1558–1566.

(16) Wu, S.-C.; Lu, C.-Y.; Chen, Y.-L.; Lo, F.-C.; Wang, T.-Y.; Chen, Y.-J.; Yuan, S.-S.; Liaw, W.-F.; Wang, Y.-M. Water-Soluble Dinitrosyl Iron Complex (DNIC): A Nitric Oxide Vehicle Triggering Cancer Cell Death via Apoptosis. *Inorg. Chem.* **2016**, *55* (18), 9383–9392.

(17) Keszler, A.; Lindemer, B.; Hogg, N.; Weihrauch, D.; Lohr, N. L. Wavelength-dependence of vasodilation and NO release from S-nitrosothiols and dinitrosyl iron complexes by far red/near infrared light, *Archives Biochem. Biophys*. **2018**, *649,* 47-52

(18) Vithayathil, A. J.; Ternberg, J. L.; Commoner, B. Changes in Electron Spin Resonance Signals of Rat Liver during Chemical Carcinogenesis. *Nature* **1965**, *207* (5003), 1246–1249.

(19) Vanin, A. F.; Nalbandian, R. M. Free Radicals of a New Type in Yeast Cells. *Biofizika* **1965**, *10*, 167–168.

(20) Tsai, M.-L.; Tsou, C.-C.; Liaw, W.-F. Dinitrosyl Iron Complexes (DNICs): From Biomimetic Synthesis and Spectroscopic Characterization toward Unveiling the Biological and Catalytic Roles of DNICs. *Acc. Chem. Res.* **2015**, *48* (4), 1184–1193.

(21) Bulter, A.R.; Megson, I. L. Non-Heme Iron Nitrosyls in Biology, *Chem. Rev*. **2002,** *102* (4), 1155-1166.

(22) Li, L.; Li, L. Recent Advances in Multinuclear Metal Nitrosyl Complexes. *Coord. Chem. Rev.* **2016**, *306*, 678–700.

(23) Conrado, C. L.; Bourassa, J. L.; Egler, C.; Wecksler, S.; Ford, P. C. Photochemical Investigation of Roussin's Red Salt Esters: Fe2(μ-SR)2(NO)4. *Inorg. Chem.* **2003**, *42* (7), 2288–2293.

(24) Vanin, A. F.; Poltorakov, A. P.; Mikoyan, V. D.; Kubrina, L. N.; Burbaev, D. S. Polynuclear Water-Soluble Dinitrosyl Iron Complexes with Cysteine or Glutathione Ligands: Electron Paramagnetic Resonance and Optical Studies. *Nitric Oxide* **2010**, *23* (2), 136–149.

(25) Pereira, J. C. M.; Iretskii, A. V.; Han, R.-M.; Ford, P. C. Dinitrosyl Iron Complexes with Cysteine. Kinetics Studies of the Formation and Reactions of Dnics in Aqueous Solution. *J. Am. Chem. Soc.* **2015**, *137* (1), 328–336.

(26) Muller, B.; Kleschyov, A. L.; Stoclet, J. C. Evidence for N-Acetylcysteine-Sensitive Nitric Oxide Storage as Dinitrosyl-Iron Complexes in Lipopolysaccharide-Treated Rat Aorta. *Br. J. Pharmacol.* **1996**, *119* (6), 1281–1285.

(27) Vanin, A. F. Dinitrosyl Iron Complexes and S-Nitrosothiols Are Two Possible Forms for Stabilization and Transport of Nitric Oxide in Biological Systems. *Biochemistry Mosc.* **1998**, *63* (7), 782–793.

(28) Richardson, D. R.; Lok, H. C. The Nitric Oxide–Iron Interplay in Mammalian Cells: Transport and Storage of Dinitrosyl Iron Complexes. *Biochim. Biophys. Acta* **2008**, *1780* (4), 638–651.

(29) Lok, H. C.; Sahni, S.; Jansson, P. J.; Kovacevic, Z.; Hawkins, C. L.; Richardson, D. R. A Nitric Oxide Storage and Transport System That Protects Activated Macrophages from Endogenous Nitric Oxide Cytotoxicity. *J. Biol. Chem.* **2016**, *291* (53), 27042–27061.

(30) Sahni, S.; Hickok, J. R.; Thomas, D. D. Nitric Oxide Reduces Oxidative Stress in Cancer Cells by Forming Dinitrosyliron Complexes. *Nitric Oxide* **2018**, *76*, 37–44.

(31) Li, Q.; Li, C.; Mahtani, H. K.; Du, J.; Patel, A. R.; Lancaster, J. R. Nitrosothiol Formation and Protection against Fenton Chemistry by Nitric Oxide-Induced Dinitrosyliron Complex Formation from Anoxia-Initiated Cellular Chelatable Iron Increase. *J. Biol. Chem.* **2014**, *289* (29), 19917–19927.

(32) Bosworth, C. A.; Toledo, J. C.; Zmijewski, J. W.; Li, Q.; Lancaster, J. R. Dinitrosyliron Complexes and the Mechanism(s) of Cellular Protein Nitrosothiol Formation from Nitric Oxide. *Proc. Natl. Acad. Sci. U.S.A.* **2009**, *106* (12), 4671–4676.

(33) Truzzi, D. R.; Augusto, O.; Ford, P. C. Thiyl Radicals Are Co-Products of Dinitrosyl Iron Complexes (DNICs) Formation. *Chem. Commun.* **2019**, 55, 9156-9159.

(34) Botello-Mort, L.; Fillat, M. Thiol-Based Redox Regulators in Prokaryotes: The Relevance of the CXXC Motifs.OA Biochemistry. *OA Biochemistry* **2014**, *18* (2), 1–8.

(35) Laurindo, F. R. M.; Pescatore, L. A.; de Castro Fernandes, D. Protein Disulfide Isomerase in Redox Cell

Signaling and Homeostasis. *Free Radical Biology and Medicine* **2012**, *52* (9), 1954–1969.
(36) Quan, S.; Schneider, I.; Pan, J.; Von Hacht, A.; Bardwell, J. C. A. The CXXC Motif Is More than a Redox Rheostat. *Journal of Biological Chemistry* **2007**, *282* (39), 28823–28833.
(37) Vanin, A. F. Dinitrosyl Iron Complexes with Thiolate Ligands: Physico-Chemistry, Biochemistry and Physiology. *Nitrix Oxide* **2009**, *21* (1), 1–13.
(38) Wanat, A.; Schneppensieper, T.; Stochel, G.; van Eldik, R.; Bill, E.; Wieghardt, K. Kinetics, Mechanism, and Spectroscopy of the Reversible Binding of Nitric Oxide to Aquated Iron(II). An Undergraduate Text Book Reaction Revisited. *Inorg Chem* **2002**, *41* (1), 4–10.
(39) The formal iron oxidation state in a DNIC such as $Fe(NO)_2(RS)_2$, is somewhat controversial (See Ref 25). If one considers the nitrosyls as neutral NOs, this leaves the iron in the +1 oxidation State; however, the electronic structures of metal nitrosyl complexes are highly delocalized, so such formalism is simply electron bookkeeping and may not imply specific reactivity properties.
(40) Kuzmic, P. Program DYNAFIT for the Analysis of Enzyme Kinetic Data: Application to HIV Proteinase. *Anal. Biochem.* **1996**, *237* (2), 260–273.
(41) Kuzmič, P. DynaFit—A Software Package for Enzymology. *Meth. Enzymol.*; Elsevier, **2009**; 467, 247–280.
(42) Another way of estimating ε_{B350} is to assume that when the transient absorbance at 450 nm reaches its maximum value, the primary Fe(II) species present Is **B**. From examining the spectrum at this juncture, an estimate of $(6.4 \pm 0.7) \times 10^3$ M^{-1} cm^{-1} was obtained. The agreement Is quite reasonable.
(43) Tajc, S. G.; Tolbert, B. S.; Basavappa, R.; Miller, B. L. Direct Determination of Thiol PKa by Isothermal Titration Microcalorimetry. *J. Am. Chem. Soc.* **2004**, *126* (34), 10508–10509.
(44) Nalwaya, N.; Deen, W. M. Nitric Oxide, Oxygen, and Superoxide Formation and Consumption in Macrophage Cultures. *Chem. Res. Toxicol.* **2005**, *18* (3), 486–493.
(45) Lancaster, J. R. Nitroxidative, Nitrosative, and Nitrative Stress: Kinetic Predictions of Reactive Nitrogen Species Chemistry Under Biological Conditions. *Chem. Res. Toxicol.* **2006**, *19* (9), 1160–1174.
(46) Damasceno, F. C.; Condeles, A. L.; Lopes, A. K. B.; Facci, R. R.; Linares, E.; Truzzi, D. R.; Augusto, O.; Toledo, J. C. The Labile Iron Pool Attenuates Peroxynitrite-Dependent Damage and Can No Longer Be Considered Solely a pro-Oxidative Cellular Iron Source. *J. Biol. Chem.* **2018**, *293* (22), 8530–8542.
(47) Hess, D. T.; Stamler, J. S. Regulation by S-Nitrosylation of Protein Post-Translational Modification. *J. Biol. Chem.* **2012**, *287* (7), 4411–4418.
(48) Smith, B. C.; Marletta, M. A. Mechanisms of S-Nitrosothiol Formation and Selectivity in Nitric Oxide Signaling. *Curr. Opin. Chem. Biol.* **2012**, *16* (5–6), 498–506.
(49) Lim, M. D.; Lorković, I. M.; Ford, P. C. The Preparation of Anaerobic Nitric Oxide Solutions for the Study of Heme Model Systems in Aqueous and Nonaqueous Media: Some Consequences of NO x Impurities. *Meth. Enzymol.* **2005**, *396*, 3–17.
(50) *Oxides of Nitrogen*, 1st ed.; Young, C. L., Ed.; Solubility data series; Pergamon Press: Oxford; New York, 1981.
(51) Mendes, P. Biochemistry by Numbers: Simulation of Biochemical Pathways with Gepasi 3. *Trends in Biochemical Sciences* **1997**, *22* (9), 361–363.
(52) Eaton, G. R.; Eaton, S. S.; Barr, D. P.; Weber, R. T. *Quantitative EPR*; Springer Vienna: Vienna, 2010.
(53) Richardson, D. R.; Lok, H. C. The Nitric Oxide–Iron Interplay in Mammalian Cells: Transport and Storage of Dinitrosyl Iron Complexes. *Biochim. Biophys. Acta* **2008**, *1780* (4), 638–651.

Table of Contents Graphic